AIAA JOURNAL
Vol. 37, No. 9, September 1999

Accuracy of Shock Capturing in Two Spatial Dimensions

Mark H. Carpenter*
NASA Langley Research Center, Hampton, Virginia 23681-0001
and
Jay H. Casper†
Old Dominion University, Norfolk, Virginia 23529

An assessment of the accuracy of shock-capturing schemes is made for two-dimensional steady flow around a cylindrical projectile. Both a linear fourth-order method and a nonlinear third-order method are used in this study. This study shows, contrary to conventional wisdom, that captured two-dimensional shocks are asymptotically first order, regardless of the design accuracy of the numerical method. The practical implications of this finding are discussed in the context of the efficacy of high-order numerical methods for discontinuous flows.

I. Introduction

HIGH-ORDER schemes (schemes of second-order accuracy or higher) have been used effectively to capture shocks for at least 30 years.[1] Little doubt remains in regard to the advantages of these schemes over the first-order schemes. For this reason, second- and higher-order schemes have almost universally replaced first-order schemes throughout computational fluid dynamics (CFD). Although there are earlier works that address the first-order nature of shock-capturing methods (see Ref. 2 or 3), only recently has a critical analysis of the actual error of higher-order schemes been undertaken within the shock-capturing community. Previous work by Casper and Carpenter[4] shows that time-dependent shocks can only be captured with first-order accuracy, regardless of the design order of the numerical method. Figure 1 shows the pointwise error from a sound–shock interaction problem, for which a fourth-order nonlinear essentially nonoscillatory (ENO) algorithm is used to solve the time-dependent Euler equations. Figure 2 shows the same problem resolved with a sixth-order linear finite difference algorithm. Both algorithms converge at a first-order rate downstream of the shock. This degradation in accuracy is caused by the inability of conventional numerical methods to pass information through a discontinuity.

In a companion work,[5] these results are reaffirmed and quantified for a broader class of problems. Specifically, a sixth-order-accurate compact implicit finite difference scheme and a fourth-order-accurate ENO scheme are used to investigate various discontinuous flows. The design order of accuracy is achieved in the smooth regions of a steady-state, quasi-one-dimensional Euler test case, as well as in the time-dependent Burgers' equation. However, in an unsteady Euler sound–shock interaction problem, first-order results are obtained downstream of the shock. A discontinuous linear model problem identifies the cause of the first-order results and quantifies the error as predominantly a numerical phase shift that results from information passing through the discontinuity. Postprocessing the first-order data increases the solution accuracy downstream of the discontinuity to second order, although high-order accuracy is still not attainable.

Presented as Paper 97-2107 at the AIAA 13th Computational Fluid Dynamics Conference, Snowmass Village, CO, 29 June–2 July 1997; received 19 September 1997; revision received 28 December 1998; accepted for publication 4 February 1999.

*Aerospace Engineer, Aerodynamic and Acoustic Methods Branch, MS 128; m.h.carpenter@larc.nasa.gov.

†Assistant Research Professor, Aerospace Engineering; currently Project Engineer, Hydrodynamics Group, E46, Newport News Shipbuilding, 4101 Washington Avenue, Newport News, VA 23607; casper_jh@nns.com. Associate Member AIAA.

The negative results found in one dimension can easily be extended to multiple spatial dimensions. Specifically, time-dependent shocks are inherently first-order accurate in any number of spatial dimensions. The one-dimensional steady Euler equations exhibit design accuracy away from discontinuities. Therefore, the possibility exists that the steady-state, discontinuous Euler equations will admit higher-order solutions in multiple dimensions. In this work, we quantify the solution accuracy for the steady-state two dimensional Euler equations. We show that, unlike the one-dimensional case, the two-dimensional Euler equations are first-order accurate downstream of a shock at steady state, regardless of the design accuracy of the numerical method.

In Sec. II, we present the Euler equations in two spatial dimensions. The equations are used to solve for the inviscid flow around a supersonic blunt body. In Sec. III, we describe the numerical methods used on the test problems. Three different numerical methods are used to solve for the flow around a supersonic blunt body. A Chebyshev bow-shock-fitting algorithm is used to obtain an exact solution to the problem. A linear fourth-order finite difference algorithm and a nonlinear third-order ENO numerical algorithm are used to capture the solution around the blunt body. In Sec. IV, we present a comparative study between the three methods. We show that all captured solutions are first-order accurate on sufficiently fine meshes, regardless of the design accuracy of the spatial operator. In Sec. V, we study the influence of Mach number and the effects of design accuracy on the first-order results. In Sec. VI, conclusions are given.

II. Governing Equations

We focus in this work on the two-dimensional Euler equations. In the physical coordinates, the equations are

$$\frac{\partial \boldsymbol{U}}{\partial t} + \frac{\partial \boldsymbol{F}}{\partial x} + \frac{\partial \boldsymbol{G}}{\partial y} = 0 \tag{1}$$

where

$$\boldsymbol{U} = \begin{bmatrix} \rho \\ \rho u \\ \rho v \\ \rho E \end{bmatrix}, \qquad \boldsymbol{F} = \begin{bmatrix} \rho u \\ \rho u^2 + P \\ \rho uv \\ (\rho E + P)u \end{bmatrix}, \qquad \boldsymbol{G} = \begin{bmatrix} \rho v \\ \rho vu \\ \rho v^2 + P \\ (\rho E + P)v \end{bmatrix}$$

The variables ρ, u, v, P, and E are the density, x velocity, y velocity, pressure, and total specific energy, respectively. The equation of state is

$$P = (\gamma - 1)\rho\left[E - \tfrac{1}{2}(u^2 + v^2)\right]$$

where γ is the ratio of specific heats, which is assumed to have a constant value of 1.4.

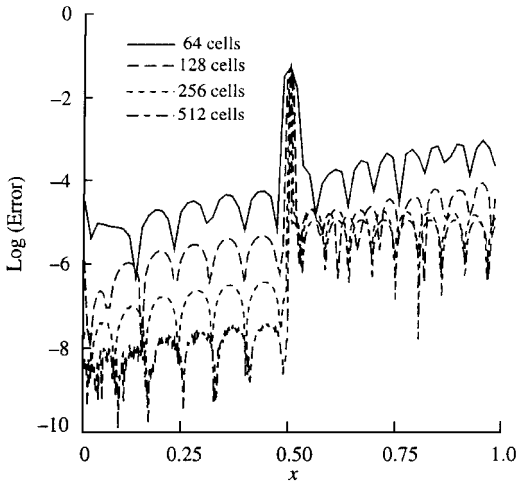

Fig. 1 Pointwise error for one-dimensional sound–shock interaction problem as obtained with nonlinear ENO-4-3 numerical scheme.

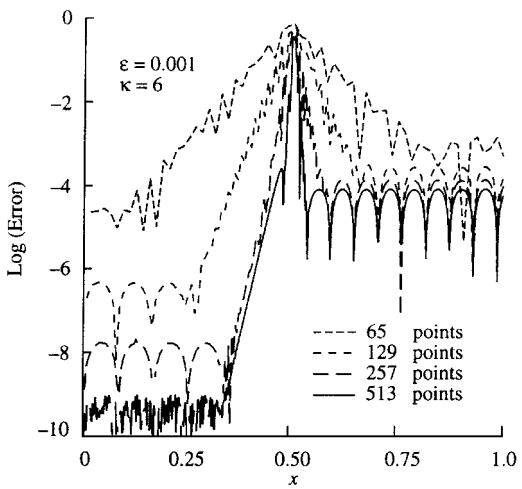

Fig. 2 Pointwise error for one-dimensional sound–shock interaction problem as obtained with linear LIN-6-4 numerical scheme.

III. Numerical Methods

We use three different numerical methods to study the two-dimensional blunt-body problem. A Chebyshev shock-fitting algorithm is used to generate an exact solution around a supersonic cylindrical projectile. Both a linear fourth-order and a nonlinear third-order ENO shock-capturing algorithm are then used to capture the solution around the cylindrical body. Accuracies are assessed by comparing the captured solutions with the exact solution. All three algorithms are fairly routine and have been documented extensively in the literature. We include a brief description of each algorithm, noting only the specific details necessary to maintain robustness on the blunt-body problem.

In assessing negative results, one must take into account the generality of the test problems and of the numerical algorithms. The two capturing algorithms represent extremes from the spectrum of higher-order formulations presently in use. We hope that this diversity adds credibility to the negative results obtained in this study.

Chebyshev Shock Fitting

A Chebyshev bow-shock-fitting algorithm is used to determine a highly accurate numerical solution to the blunt-body problem. Figure 3 shows a numerical grid wrapped around the forebody of a two-dimensional circular cylinder. A Chebyshev spatial operator is used in both the radial and the circumferential directions to resolve the inviscid flow around the cylinder. Note that the grid line farthest from the body coincides exactly with the curved bow shock.

The fitted solution is obtained by first mapping the Euler equations in space and time into the computational space. A linear mapping

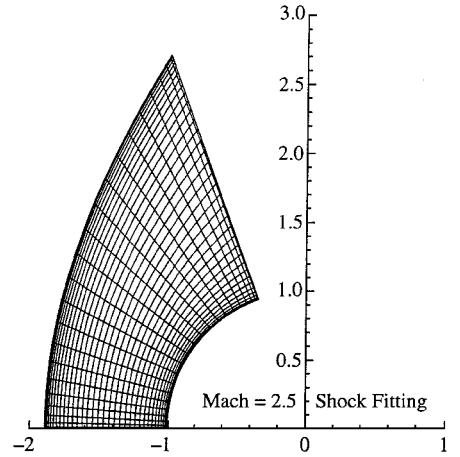

Fig. 3 Shock-fit Chebyshev spectral grid for blunt-body flow at Mach = 2.5.

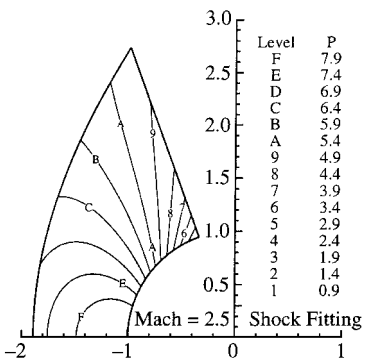

Fig. 4 Pressure profiles of exact solution obtained with Chebyshev shock-fitting algorithm.

$(r, \theta, t) \rightarrow (\xi, \eta, \tau)$ is used:

$$\xi = \frac{r - r_b(\theta)}{r_s(\theta, t) - r_b(\theta)}, \qquad \eta = \frac{\theta - \theta_{\min}}{\theta_{\max} - \theta_{\min}}, \qquad \tau = t \tag{2}$$

where r_b, r_s, $\theta_{\min}$, and $\theta_{\max}$ are the radius of the body, the radius of the shock, and the minimum and maximum values of θ, respectively. The shock position always coincides with the line $\xi = 1$, and the physical domain changes continuously as the bow shock moves to its steady-state position. Because of symmetry along the body centerline, only half of the problem is solved. The Chebyshev collocation technique is used in the computational domain to discretize the resulting set of equations. The equations are then marched in time until a steady-state solution is reached.

A crucial element of the procedure is the treatment of the boundary conditions and, in particular, the movement of the shock. To move the shock, a shock velocity equation is derived by differentiating the Rankine–Hugoniot relations at the shock. The resulting differential equations for the position and velocity of the shock are then advanced in time with a five-stage Runge–Kutta (RK) scheme, along with the rest of the discrete equations. Symmetry conditions are imposed along the centerline, and inviscid wall conditions are imposed at the body. At the outflow, the flow is supersonic normal to the boundary, and no physical boundary conditions are imposed. Further details on the boundary treatments can be found elsewhere.[6,7]

The grid used in the $M = 2.5$ case (see Fig. 3) contains 36 radial and 24 circumferential collocation points. This grid density is sufficient to predict a stagnation pressure on the centerline that is exact to 12 significant digits. The solution accuracy throughout the domain is monitored by using the spectral decay of polynomial coefficients. The worst portion of the flow is resolved to 8 orders of magnitude. This solution (referred to from now on as the exact solution) is spectrally interpolated to a sequence of uniformly spaced grids for use as error indicators in the finite difference algorithm. Figures 4–6 show the pressure, density, and velocity vector profiles of the blunt-body flow. Note the smooth, well-resolved contour lines.

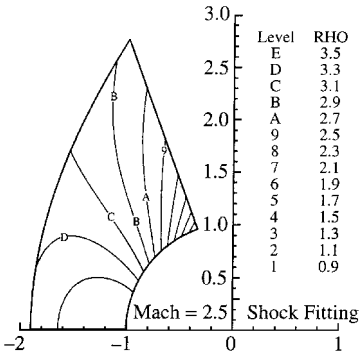

Fig. 5 Density profiles of exact solution obtained with Chebyshev shock-fitting algorithm.

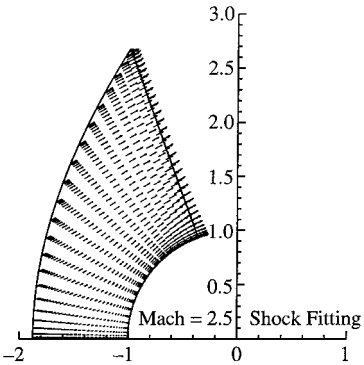

Fig. 6 Velocity vectors from the exact solution obtained with the Chebyshev shock-fitting algorithm.

Fourth-Order Linear Scheme

Conventional high-order central-difference discretizations lack the robustness necessary to efficiently converge this problem to steady state. A fourth-order upwind biased algorithm, however, proves robust and efficient over the Mach number range considered in this study. The upwinding uses a Lax–Friedrichs splitting of the flux vector. Specifically, the derivative of the contravariant flux $\hat{\boldsymbol{F}}$ is calculated as

$$D\hat{\boldsymbol{F}} = \tfrac{1}{2}(D^{+}\hat{\boldsymbol{F}}^{+} + D^{-}\hat{\boldsymbol{F}}^{-})$$

where $\hat{\boldsymbol{F}}^{\pm} = \hat{\boldsymbol{F}} \pm \lambda_{\max}\hat{\boldsymbol{U}}$ and $D^{+} = (3, 3, 3 - 4 - 3)$ and $D^{-} = (3 - 4 - 3, 3, 3)$. (The nomenclature for derivative closure D^{+}, for example, denotes that the left three points are evaluated with third-order stencils, the interior with fourth-order stencils, and the right point with a third-order stencil. Details of this nomenclature may be found elsewhere.[8]) The fourth-order D^{+} operator is the upwind-biased stencil

$$U(x_i) = \sum_{j=i-3}^{i+1} a_{i,j}U(x_j) + \mathcal{O}(\delta x)^4$$

where row i of the matrix $a_{i,j}$ is defined as $a_{i,j} = (1/12\delta x) \times [-1, 6, -18, 10, 3]$. The third-order stencils used at all boundary points are the optimal stencils derived from nearest neighbor information; these stencils are biased where possible in an upwind direction. The scaling parameter $\lambda_{\max}$ is the maximum over the entire domain of the contravariant eigenvalue $\hat{u} + \hat{c}$. A similar expression is used for the $\hat{\boldsymbol{G}}$ vector.

Historically, finite difference formulations that locate a discrete point at the stagnation point are susceptible to numerical instability. Careful implementation of the boundary conditions eliminates this problem. The present formulation is as robust as the staggered formulations that are typically adopted by finite difference algorithms near stagnation points. On the inflow plane, all variables are prescribed, which is consistent with supersonic inflow. On the outflow, the solution is simply calculated by using one-sided high-order information, and no boundary conditions are imposed. On the symmetry plane, the v component of the velocity is set to zero. On the inviscid wall, the no-penetration boundary condition is treated weakly through the flux. Specifically, the contravariant flux on the wall is calculated consistent with the no-penetration condition. (The normal velocity is flipped in sign to create a reflecting state. The two states are then rectified with a Riemann solver to obtain a state with no normal velocity.) The physical velocity at the wall is not required to satisfy the no-penetration condition. Thus, at steady state, the normal velocity at the wall is nonzero but converges to zero with an order property that is consistent with the overall formulation.

A three-stage RK scheme is used to drive the solution to steady state. The calculations are suspended when the solution error, based on the exact solution, converges to four significant places.

Third-Order Nonlinear Scheme

The third numerical scheme employed in this work is a third-order-accurate ENO algorithm. Spatial accuracy is achieved by solving the two-dimensional time-dependent Euler equations in control-volume form. Complete details of the algorithm are presented elsewhere.[9] The adaptive stencils employed in the high-order spatial operator are biased in smooth regions toward those that are linearly stable (see, for example, Ref. 10). All required mesh quantities, e.g., cell areas and grid metrics, are calculated to consistent accuracy.[9] The solution is advanced in time, toward a steady state, via a three-stage RK scheme.[11] Implicit residual smoothing is employed to accelerate the time integration.

Fluxes at cell interfaces are approximated in two distinct ways. The most accurate treatment is by Roe's approximate Riemann solver, as presented in Ref. 12. Full machine-zero convergence to steady state is not possible with this formulation. High-order accuracy is nonetheless attained on the grid-aligned test case. The robustness and generality of the formulation is somewhat questionable, which makes the use of a second formulation necessary. To drive residuals to machine zero, the Roe solver must be augmented with an entropy fix[13] and the stencils must be more heavily biased. These modifications give rise to an oscillation near the shock and cause the solution error to revert to first-order accuracy. We use the straight Roe solver as a means of verifying the accuracy of the algorithm, and the second formulation is used as the general solver in the comparative studies.

Grids

The grids used for all calculations originate from the Chebyshev spectral solution. A uniform discretization in both the radial and circumferential directions is used. To accomplish shock capturing, the grid is extended in the radial direction until exactly one-fourth of the points are in the supersonic portion of the flow. The following sequence of grids is used to perform a grid refinement study: 33×33, 65×65, 129×129, 257×257, 513×513. The exact solution is projected onto these grids (with spectral interpolation) for use as the initial condition and to calculate solution accuracies.

IV. Results

First-Order Motivation

We begin by presenting a heuristic argument that explains why the two-dimensional steady-state Euler equations admit first-order solutions downstream of two-dimensional discontinuities. We saw in previous work[4,5] that time-dependent information that passes though a discontinuity is corrupted to first order by a discontinuity. This statement was quantified using the model problem $u_t + [a(x)u]_x = 0$, where $a(x)$ is discontinuous. We concluded that first-order corruption occurs in hyperbolic equations when $a(x)$ is discontinuous with information passing through the discontinuity.

We now show that at least part of the steady-state two-dimensional Euler equations is mathematically equivalent to the model hyperbolic problem, where the wave speed $a(x)$ is discontinuous at the captured shock. (Here, the second spatial dimension takes the place of time, which results in a hyperbolic equation in x, y.) Therefore, based on the one-dimensional time-dependent results, the discontinuous two-dimensional Euler equations should exhibit first-order error downstream of an arbitrary captured discontinuity.

The equations that govern the steady-state Euler equations in two dimensions are

Table 1 Smooth test case of near-wall region that shows design accuracy of linear shock-capturing scheme

Grid	Density log L_2	4th rate	Wall boundary condition log L_2	4th rate
25×33	−3.275	——	−3.119	——
49×65	−4.230	3.17	−4.003	2.94
97×129	−5.256	3.41	−4.980	3.25
193×257	−6.330	3.57	−6.041	3.52
385×513	−7.419	3.62	−7.163	3.73

$$\frac{\partial \boldsymbol{F}}{\partial x} + \frac{\partial \boldsymbol{G}}{\partial y} = \boldsymbol{A}\frac{\partial \boldsymbol{U}}{\partial \boldsymbol{x}} + \boldsymbol{B}\frac{\partial \boldsymbol{U}}{\partial \boldsymbol{y}} = \boldsymbol{0} \tag{3}$$

where $\boldsymbol{A} = \partial \boldsymbol{F}/\partial \boldsymbol{U}$ and $\boldsymbol{B} = \partial \boldsymbol{G}/\partial \boldsymbol{U}$. The mathematical character of Eq. (3) is governed by the eigenvalues of the matrix $\boldsymbol{M} = \boldsymbol{A}^{-1}\boldsymbol{B}$. The eigenvalues of the matrix $\boldsymbol{M}$ are $\lambda_{1,2} = v/u$ and $\lambda_{3,4} = [(uv \pm a\sqrt{(u^2 + v^2 - a^2)/(u^2 - a^2)}]$. For supersonic flow, the eigenvalues are real and distinct, and the equation set is strictly hyperbolic. For subsonic flow, two of the eigenvalues are real and two are imaginary, and the equation set is mixed elliptic–hyperbolic. The two eigenvalues that are real independent of the Mach number are $\lambda_{1,2} = v/u$, and these eigenvalues correspond to the advection of information along the streamlines v/u. The mathematical character of the hyperbolic portion of the equation is identical to that exhibited in the unsteady one-dimensional equation $u_t + [a(x)u]_x = 0$, where $a(x)$ is discontinuous. Thus, the steady two-dimensional Euler equations will be of first-order accuracy downstream of any captured discontinuity.

Although the preceding argument is presented for a Cartesian coordinate system, it extends to arbitrary coordinate systems. Specifically, the fundamental hyperbolic–elliptic nature of the steady Euler equations is invariant with respect to coordinate transformations.

We digress here and note that the multidimensional accuracy at steady state is different from that found in the one-dimensional case. The one-dimensional steady-state solution is of design accuracy away from any discontinuities, whereas the two-dimensional case is of first-order accuracy behind general discontinuities. We provide no mathematical explanation for this anomaly other than to say that two dimensions are necessary to exhibit the first-order behavior.

Smooth Near-Body Problem

A model problem is needed to test the accuracy of the shock-capturing algorithms. Different formulations of the exact solution are used to test the linear and nonlinear algorithms. We begin by describing the testing of the linear algorithm.

By solving for the flow between the bow shock and the cylinder (the near body), we test the centerline, wall, and outflow boundary conditions, as well as the design accuracy of the method. Because no discontinuities are present in this subproblem, the linear formulation should recover design accuracy. If the grid points are eliminated outside the bow shock, then a subsequence of grids is formed with 25×33, 49×65, 97×129, 193×257, and 385×513 points, respectively. The boundary conditions for the centerline, wall, and outflow planes are identical to those described earlier. The subsonic inflow boundary condition at the bow shock is implemented by solving the Riemann problem between the numerical state at the point and the exact postshock conditions from the spectral algorithm.

Table 1 shows the results of a grid-refinement study in which the linear fourth-order scheme is used for $M = 2.5$. Reported are the L_2 error in density and the L_2 error in the normal velocity component at the inviscid wall, both as a function of grid. The L_2 error is defined as

$$L_2 = \sqrt{\frac{\sum_i^N \left(\psi_i - \psi_i^{\text{ex}}\right)^2}{N}}$$

where ψ_i and ψ_i^{ex} are the numerical and exact values of the respective functions at point i and N is the number of points in the norm. The norm of density is formed over the entire domain. (The norm of wall-normal velocity is formed over all body points.)

Table 2 Special fitted test case that shows design accuracy of ENO formulation with standard Roe flux at interfaces

Grid	Density log L_2	3rd rate
33×33	−3.162	——
65×65	−4.042	2.92
129×129	−5.007	3.21
257×257	−6.045	3.45

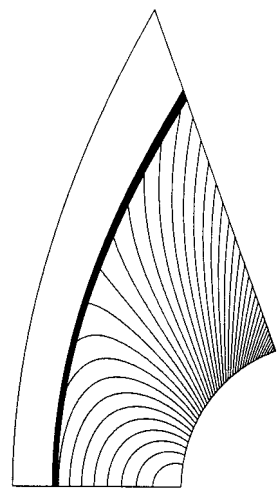

Fig. 7 Density profiles of the captured solution obtained with the third-order ENO method, using only the Roe flux at the interfaces; solution is third-order accurate.

The convergence rate asymptotes to the theoretical value of 4. (The third-order closure near the boundaries dominates the solution accuracy on the coarse grids.) The normal component of the velocity at the wall goes to zero in accordance with the weak imposition of the tangency condition. Similar convergence behavior is observed for the pressure and for other norms.

Several specific features of the blunt body and the ENO formulation allow for a convincing test of the nonlinear formulation. The full grid is constructed such that the shock coincides exactly with an interface in the finite volume formulation. If smooth interpolants are used on either side of the cell interface and a Riemann solver that satisfies the Rankine–Hugoniot shock jump relations is used, then for this special case the shock is fit at the cell interface. All constraints are met by the ENO formulation with a Roe flux at the interfaces. As noted earlier, the temporal residual for this test problem does not converge more than four orders of magnitude. Nevertheless, design accuracy is achieved on the original sequence of four grids.

Table 2 shows the results of a grid refinement study in which the third-order ENO scheme is used for $M = 2.5$. The L_2 error in density is reported; the definitions of error are the same as were reported for the linear case.

The convergence rate asymptotes to a value that is greater than the theoretical accuracy of 3. Note that in an absolute sense the errors from the third-order ENO formulation are comparable with those obtained from the fourth-order linear algorithm. The two-dimensional of the pressure and density obtained from the ENO algorithm are nearly indistinguishable from the exact solutions shown in Figs. 4 and 5. Figure 7 shows the pressure profiles that are obtained with the nonlinear ENO algorithm for this test case. (Note the monotone one-point bow shock.)

Several points can be deduced from these studies. First, the shock-capturing algorithms exhibit design accuracy on the near-body subproblem. This finding indicates that the symmetry, wall, and outflow boundaries are correct. Second, the agreement to seven significant digits between the capturing algorithm and the Chebyshev spectral solution indicates that the exact answer is correct to at least seven digits.

Shock-Captured Blunt-Body Problem

We now use the validated linear fourth-order and the nonlinear third-order algorithms to capture the bow shock around a Mach 2.5

Table 3 Captured Mach 2.5 bow shock around circular cylinder with linear shock-capturing scheme

Grid	Density log L_2	4th rate	Pressure log L_2	4th rate
33×33	−1.756	——	−1.651	——
65×65	−3.404	5.47	−3.370	5.74
129×129	−3.708	1.01	−3.778	1.32
257×257	−4.014	1.02	−4.117	1.13
513×513	−4.317	1.01	−4.437	1.06

Table 4 Captured Mach 2.5 bow shock around circular cylinder with third-order ENO shock-capturing scheme

Grid	Density log L_2	3rd ENO rate
33×33	−2.275	——
65×65	−2.572	0.99
129×129	−2.871	0.99
257×257	−3.170	0.99

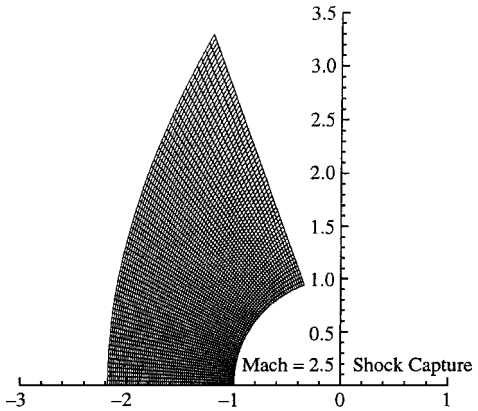

Fig. 8 Finite difference grid that employs 65 × 65 evenly spaced points, used to capture blunt-body flow for $M = 2.5$.

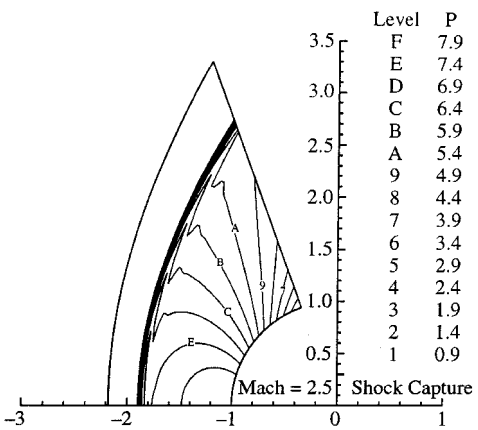

Fig. 9 Pressure profiles of captured solution obtained with fourth-order finite difference algorithm.

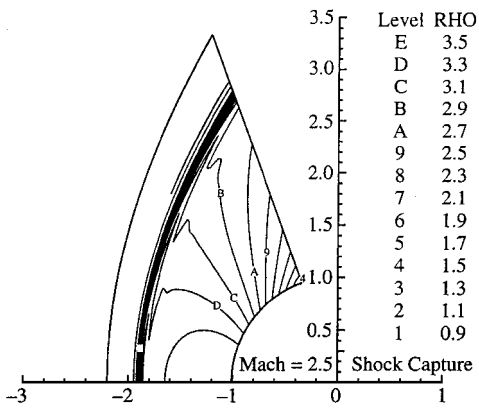

Fig. 10 Density profiles of captured solution obtained with fourth-order finite difference algorithm.

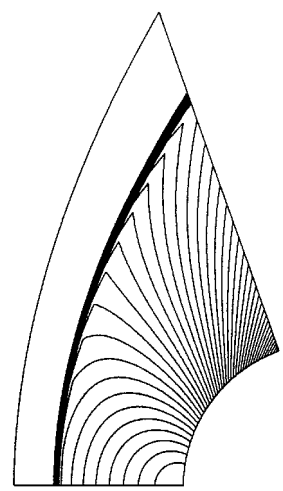

Fig. 11 Density profiles of captured solution obtained with third-order ENO algorithm by using Roe flux with entropy fix at interfaces; solution is first-order accurate.

circular cylinder. Only two modifications are necessary to capture the blunt-body shock. First, in the linear formulation the original grids are used, and supersonic freestream conditions are imposed at the inflow. Second, for the nonlinear ENO formulation, the Roe solver at the interfaces is modified with an entropy fix, and the stencil-biasing parameters are tuned. These modifications allow a steady-state residual to be driven to machine precision but eliminate the possibility of fitting the shock at the interface.

Figure 8 shows the 65×65 grid used in both formulations. Figures 9 and 10 show the two-dimensional pressure and density profiles that are obtained with the linear method. Figure 11 shows the pressure profiles obtained with the nonlinear method. All profiles are obtained on the 65×65 grid. The solution from the linear algorithm has huge oscillations at the captured shock, whereas the nonlinear formulation is nearly monotone.

Tables 3 and 4 present refinement studies for which the original sequence of grids is used. In Table 3, the L_2 norms of the density and pressure errors are presented, as obtained with the fourth-order linear algorithm. The density and pressure norms are formed by using only the half of the domain that is closest to the body to exclude any points close to the captured-shock region.

In marked contrast to the accuracy of the near-body problem, the two-dimensional captured-shock accuracy is asymptotically first order in space. On coarse grids, the scheme converges near the design accuracy but is dominated by the first-order shock error on finer grids. Note that the density and pressure exhibit nearly identical behavior. We note but do not show here that the wall penetration error is asymptoting to design accuracy as it did in the near-wall test problem.

In Table 4, the L_2 norm of the density error is presented, as obtained with the third-order ENO algorithm. The same error norm is used here as for the linear algorithm. The two-dimensional captured-shock accuracy is asymptotically first order in space. The nonlinear formulation yields increased accuracy on coarse grids but, surprisingly, is less accurate asymptotically than the fourth-order linear algorithm. Not surprisingly, no component of high-order convergence exists for this problem, unlike the linear scheme. Work continues with the nonlinear scheme to recover better asymptotic error behavior at steady state. Based on previous experience with the nonlinear formulation, the asymptotic error level can be reduced by further optimization of the biasing parameters and the entropy fix.

By comparing the near-body and blunt-body solution errors, we establish that capturing the discontinuity in the blunt-body case causes a degradation in accuracy. The resulting convergence rate is first order for both the linear and nonlinear formulations. We claim that this result is general for any multidimensional shock and any high-order numerical method. A heuristic explanation for this phenomenon is related to the ambiguous shock position within the cell. Capturing the shock provides (through conservation and the Rankine–Hugoniot relation) the postshock conditions for the smooth near-body problem. Because the exact position of the shock is ambiguous to order δx, these numerical conditions are incorrect to first order. This first-order error is relatively small on coarse grids but at some level of refinement becomes the dominant error term.

A possible exception to the first-order conclusion is the case in which a multidimensional shock can be one dimensionalized by a suitable rotation. For example, if the numerical grid is aligned with the shock throughout the domain and the Roe solver is used to rectify the interface states, then design accuracy is possible at steady state. Rotating a shock into a one-dimensional reference frame is roughly equivalent to shock fitting and is a formidable task in general situations. In spite of these difficulties, some progress has been made recently.[14,15]

V. First-Order Implications

We have demonstrated that captured shocks in two dimensions are first order regardless of the design accuracy of the capturing scheme. At some point of spatial resolution, the solution is dominated by the first-order component of the error, which raises an obvious question. If the solution error is bounded at first order, then to what extent should high-order formulations be considered for capturing discontinuous flows? Specifically, for what class of problems does the first-order error component dominate the solution error, making additional high-order work counterproductive? We first present a parametric study of design accuracy to quantify the nature of the first-order error component. We then begin to address the specific role of high-order algorithms in the context of shock capturing.

Dependence of Error on Design Accuracy

Tables 5–7 compare different design accuracies for the Mach 2.5 blunt-body problem. The study is performed by the linear algorithm. Work continues with the nonlinear algorithm to quantify the generality of the conclusions drawn in this study. We include spatial operators of first-, second-, and fourth-order accuracy. The fourth-order pressure and density results shown earlier are compared with those obtained with the second- and first-order algorithms. We see that all methods are asymptotically first order. The results from the first-order (design accuracy) scheme are very poor, and only a partial listing is included. Note that the asymptotic level of error in the second- and fourth-order schemes is the same. The first-order component of the captured error appears to be nearly independent of the design order of accuracy of the method. The fourth-order scheme quickly approaches the asymptotic limit; the second-order scheme asymptotes more slowly. The first-order (design accuracy) scheme will never be dominated by shock error.

Table 5 Fourth-order linear algorithm

Grid	Density log L_2	4th rate	Pressure log L_2	4th rate
33×33	−1.756	——	−1.651	——
65×65	−3.404	5.47	−3.370	5.74
129×129	−3.708	1.01	−3.778	1.32
257×257	−4.014	1.02	−4.117	1.13
513×513	−4.317	1.01	−4.437	1.06

Table 6 Second-order linear algorithm

Grid	Density log L_2	2nd rate	Pressure log L_2	2nd rate
33×33	−2.327	——	−2.087	——
65×65	−2.776	1.49	−2.933	2.81
129×129	−3.242	1.55	−3.664	2.43
257×257	−3.660	1.39	−4.321	2.18
513×513	−4.034	1.24	−4.452	0.44

Table 7 First-order linear algorithm used to capture the Mach 2.5 bow shock around supersonic circular cylinder

Grid	Density log L_2	1st rate	Pressure log L_2	1st rate
33×33	−0.891	——	−0.745	——
65×65	−1.335	1.47	−1.049	1.01
129×129	−1.683	1.16	−1.348	0.99
257×257	−2.040	1.19	−1.652	1.01

A heuristic model that expresses the nature of the solution error that is exhibited by the linear schemes must include a first-order and a design-order component. A model that is approximately consistent with the solution errors presented in Tables 5–7 is

$$\epsilon = c_1(\delta x)^1 + c_2(\delta x)^r \tag{4}$$

where ϵ is the solution error, r is the design order of the numerical algorithm, and c_1 and c_2 are problem-dependent constants. For $r > 1$ and any finite values c_1 and c_2, the solution error will asymptotically be dominated by the first-order error component. If $c_1 \ll c_2$, the solution will exhibit high-order convergence on coarse grids.

Role of High-Order Shock Capturing

Practitioners are interested in absolute error, rather that the order of the spatial approximation. Order of accuracy and absolute error are closely related in the asymptotic limit of high accuracy. Most engineering problems, however, require error levels far removed from this asymptotic limit. Thus, a second-order algorithm could converge at its design rate for many target accuracies. Thus, the first-order convergence of captured shocks has largely been overlooked, much less quantified, over the past 30 years.

As computers become more powerful, practitioners demand more accuracy from their calculations. In aeroacoustics and electromagnetics, demands to resolve scales that differ by several orders of magnitude are commonplace. In configuration aerodynamics, a commonly used metric of solution accuracy for viscous airfoils is one drag count, which corresponds to solution accuracies of at least four significant digits. As the design accuracy requirements increase, the solution error is more likely to be dominated by the first-order component downstream of a discontinuity. When this occurs, global refinement of the solution is no longer a viable procedure; local refinement of the shock region must be performed to obtain an accurate solution.

In an attempt to quantify these generalizations, we begin by noting that the overall impact of shock capturing error depends not only on absolute shock error, but also on the position and prominence of the shock. Only those portions of the domain where information propagates through the shock are subject to shock-capturing error. Thus, if this domain of dependence is not prominent, then errors in shock position or strength will have little impact on the overall solution accuracy or derived quantities. For example, note that in many transonic airfoil calculations, only a small portion of the upper surface is subject to first-order errors. As such, high-order numerical methods are an obvious candidate for resolving these flows.

For those problems where accurate resolution of a prominent shock is crucial, one must determine the magnitude of shock-capturing error that is acceptable. We now show that shock-capturing error depends on flow conditions and generally increases with increasing shock strength.

We present a study with Mach number as a parameter, in which the linear algorithms of fourth-, second-, and first-order accuracy are used. The objective of the study is to show that the efficacy of high-order methods is dependent on the problem, as well as the target accuracy level. Figure 12 shows a plot of the pressure data that are presented in Table 5. Lines of unit slope are included to compare the asymptotic convergence rates of the methods. On this plot, the method that is the most efficient for a given target accuracy can more

Table 8 Centerline, bow-shock, density, and pressure ratios, as function of Mach number

Mach	Density	Pressure
2.0	2.667:1	4.500:1
2.5	3.333:1	7.125:1
3.0	3.857:1	10.333:1

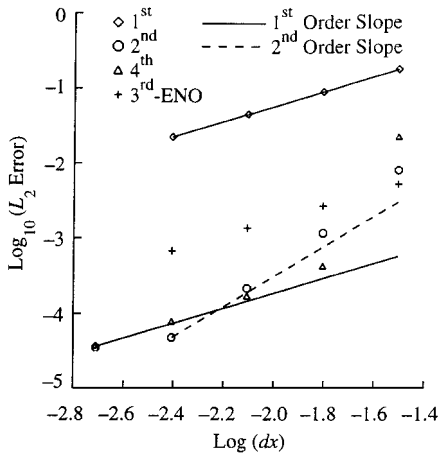

Fig. 12 Grid refinement study at Mach = 2.5 showing dependence of solution error on the design accuracy of the numerical scheme.

easily be identified. At a target accuracy of 10^{-2}, the second-order scheme is most desirable. (On the coarsest grid, the second-order scheme is more accurate than the fourth-order scheme.) At a target of 10^{-3}, the fourth-order scheme is most desirable. At one drag count or four significant digits (10^{-4}), both methods are in the first-order asymptotic limit. Neither method is computationally efficient, and refinement of the grid in the bow-shock region would be the best use of computer resources.

The results in Fig. 12 are consistent with the observation that in many circumstances the first-order shock component of the solution error is negligibly small. Note that the second-order scheme is profoundly more accurate than the first-order scheme and only begins to show its first-order character on extremely fine grids. Seldom have accuracy levels comparable to those reported here been obtained by CFD practitioners because of the costs involved; thus, the first-order nature of the captured solution has not been uniformly recognized until now.

Figures 13 and 14 show results for Mach numbers of 2 and 3, respectively. The three numerical schemes used in the case where $M = 2.5$ are used in these studies. Table 8 shows the shock strengths as a function of Mach number for the range $2 \leq M \leq 3$. The conclusions drawn in the case for which $M = 2.5$ appear to be reasonably general for this range of Mach numbers. Specifically, the first-order (design accuracy) results are not competitive with either the second- or fourth-order results. Both higher-order methods exhibit design accuracy on coarse grids, but asymptote to first order on fine grids. The asymptotic level of the higher-order schemes is nearly independent of the design accuracy. At low target accuracies, the second-order scheme is most desirable, and at moderate target accuracies, the fourth-order scheme is most desirable. At high target accuracies, the high-order schemes are first order because of the shock, and regridding the shock is necessary to effectively decrease the overall accuracy of the calculation.

The convergence rates at all Mach numbers are consistent with the heuristic model proposed in Eq. (4). We do see a slight dependence of the asymptotic first-order shock error on the shock strength, which increases with Mach number. Note that shocks of infinitesimal strength produce smooth errors with no first-order component. In an attempt to cast these results in a global perspective, we re-examine the case of the transonic airfoil. We noted earlier that these airfoils exhibit predominantly smooth flow and, as such, are not likely candidates for dominant shock-capturing errors. This fact,

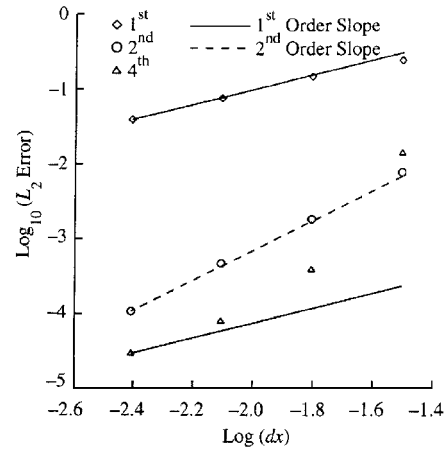

Fig. 13 Grid refinement study at Mach = 2.0 showing dependence of solution error on the design accuracy of the numerical scheme.

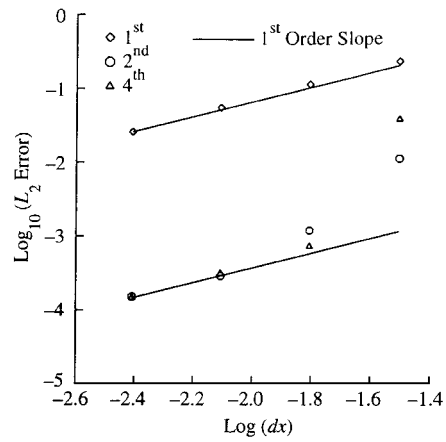

Fig. 14 Grid refinement study at Mach = 3.0 showing dependence of solution error on the design accuracy of the numerical scheme.

coupled with the low shock-capturing errors expected from weak shocks, leads one to the conclusion that any first-order error component will be small and will not dominate the solution accuracy for accuracy requirements of one drag count. Nevertheless, work continues to quantify the nature of captured shocks and to predict the shock-capturing error levels at the shock. This quantification hopefully will provide some general guidance in capturing shocks of different strengths and in refining the shock to ensure satisfactory results near the body.

VI. Conclusions

An assessment of the accuracy of shock-capturing schemes is made for two-dimensional steady flows. A linear fourth-order method and a nonlinear third-order method are used in this study. Results show, contrary to conventional wisdom, that captured two-dimensional shocks are asymptotically first order, regardless of the design accuracy of the numerical method that is used to obtain them.

The solution error of the captured discontinuity can be characterized by a first-order component $c_1(\delta x)^1$ and a high-order component $c_2(\delta x)^r$ (where r is the design order of the method). With sufficient resolution, the error is dominated by the first-order terms. In a practical sense, however, the solution error is frequently dominated by the high-order component, which gives the appearance of a high-order convergence rate.

Finally, we acknowledge that demonstrating a first-order convergence rate with two numerical methods does not prove that captured shocks are destined only to be first-order accurate. Rather, this research demonstrates that we do not presently know how to achieve high-order convergence in a general context when discontinuities are present. Work continues toward achieving the goal of design accuracy for captured discontinuities.

Acknowledgment

This work was supported in part by U.S. Government Grant NAG1-1653.

References

[1]MacCormack, R. W., "The Effects of Viscosity in Hypervelocity Impact Cratering," AIAA Paper 69-354, April 1969.

[2]Majda, A., and Osher, S., "Propagation of Error in Regions of Smoothness for Accurate Difference Approximations to Hyperbolic Equations," *Communications in Pure and Applied Mathematics*, Vol. 30, Nov. 1977, pp. 671–705.

[3]Mock, M. S., and Lax, P. D., "The Computation of Discontinuous Solutions of Linear Hyperbolic Equations," *Communications in Pure and Applied Mathematics*, Vol. 31, No. 4, 1978, pp. 423–430.

[4]Casper, J., and Carpenter, M. H., "Computational Considerations for the Simulation of Shock-Induced Sound," *SIAM Journal on Scientific Computing*, Vol. 19, No. 3, 1998, pp. 813–828.

[5]Carpenter, M. H., and Casper, J., "Computational Considerations for the Simulation of Discontinuous Flows," *Barriers and Challenges in Computational Fluid Dynamics*, edited by V. Venkatakrishnan, Kluwer Academic, Norwell, MA, 1997, pp. 63–78.

[6]Kopriva, D. A., "Spectral Methods for the Euler Equations: The Blunt-Body Problem Revisited," *AIAA Journal*, Vol. 29, No. 9, 1991, pp. 1458–1462.

[7]Carpenter, M. H., Atkins, H. L., and Singh, D. J., "Characteristic and Finite-Wave Shock-Fitting Boundary Conditions for Chebyshev Methods," *Transition, Turbulence, and Combustion*, edited by M. Y. Hussaini, T. B. Gatski, and T. L. Jackson, Vol. 2, Kluwer Academic, Norwell, MA, 1994, pp. 301–312.

[8]Carpenter, M. H., Gottlieb, D., and Abarbanel, S., "The Stability of Numerical Boundary Treatments for Compact High-Order Finite-Difference Schemes," *Journal of Computational Physics*, Vol. 108, No. 2, 1993, pp. 272–295.

[9]Casper, J., and Atkins, H., "A Finite-Volume High-Order ENO Scheme for Two-Dimensional Hyperbolic Systems," *Journal of Computational Physics*, Vol. 106, No. 1, 1993, pp. 62–76.

[10]Casper, J., Shu, C., and Atkins, H., "A Comparison of Two Formulations for High-Order Accurate Essentially Nonoscillatory Schemes," *AIAA Journal*, Vol. 32, No. 10, 1994, pp. 1970–1977.

[11]Shu, C., and Osher, S., "Efficient Implementation of Essentially Non-Oscillatory Shock-Capturing Schemes," *Journal of Computational Physics*, Vol. 77, No. 2, 1988, pp. 439–471.

[12]Roe, P. L., "Approximate Riemann Solvers, Parameter Vectors, and Difference Schemes," *Journal of Computational Physics*, Vol. 43, Oct. 1981, pp. 357–372.

[13]Harten, A., Lax, P., and Van Leer, B., "On Upstream Differencing and Godunov-Type Schemes for Hyperbolic Conservation Laws," *SIAM Review*, Vol. 25, No. 1, 1983, pp. 35–61.

[14]Paraschivoiu, M., Trepanier, J. Y., Reggio, M., and Camarero, R., "A Conservative Dynamic Discontinuity Tracking Algorithm for the Euler Equations," AIAA Paper 94-0081, Jan. 1994.

[15]van Rosendale, J., "Floating Shock Fitting via Lagrangian Adaptive Meshes," AIAA Paper 95-1721, June 1995.

D. S. McRae
Associate Editor